Phonon Frequencies in NaBr†

J. S. Reid and T. Smith
Department of Natural Philosophy, The University, Aberdeen, Scotland

AND

W. J. L. Buyers
Chalk River Nuclear Laboratories, Atomic Energy of Canada Limited, Chalk River, Ontario, Canada

(Received 7 July 1969)

The frequencies of phonons in NaBr at 295°K propagating along the [001], [110], and [111] directions have been obtained from measurements of slow-neutron scattering made with a time-of-flight spectrometer and with a triple-axis spectrometer. The results have been fitted by least-squares techniques to both rigid-shell and deformable-shell models. The most satisfactory fit is obtained using a rigid-shell model with six disposable parameters and no second-neighbor force constants. Frequencies given by a variety of models with parameters determined by macroscopic constants are compared with the measured frequencies, and the effect of using zero-sound elastic constants is examined. The agreement is comparable to that found in other polarizable alkali halides. Finally, the frequency distribution at room temperature is obtained, and the temperature dependence of the specific heat and of the reduced moments are calculated with allowance for temperature-dependent quasiharmonic frequencies.

INTRODUCTION

Among the alkali halides the lattice dynamics of NaBr is of interest because the extreme deviations from the Szigeti relations[1] for effective charge and compressibility suggest that the deformation of the electron distribution is particularly important. The effective charge e^*/e calculated from recent low-temperature parameters[2,3] has the low value of 0.73 while the compressibility k^*/k is 1.05 at room temperature and 1.15 at 0°K.

The present phonon frequency measurements complement those already made on the alkali halides KBr,[4] NaI,[4] KI,[5] NaCl,[6] LiF,[7] and NaF.[8] The measurements reported here were made with a conventional triple-axis spectrometer and a time-of-flight spectrometer.[9] The wave vector and frequency coordinates $(\mathbf{q},\omega)$ of the phonons involved in the coherent scattering of slow neutrons with incident wave vector k_0 and mass m from the state $(\hbar\mathbf{k}_0,\hbar^2k_0^2/2m)$ to the state $(\hbar\mathbf{k}, \hbar^2k^2/2m)$ were deduced from the conservation equations

$$\mathbf{k}_0-\mathbf{k}=\mathbf{G}-\mathbf{q}=\mathbf{Q}, \quad (1)$$

$$k_0^2-k^2=(2m/\hbar)\omega, \quad (2)$$

where $\mathbf{G}$ is a reciprocal-lattice vector.

The frequencies determined from the experiment were compared with those predicted from two sets of harmonic interionic force models. The parameters of the first set were obtained by least-squares fitting to the measured frequencies. The parameters of the other set were derived from macroscopic measurements. In both cases the effect of allowing radial deformations of the ions[10] was considered. Also, the deformable dipole model of Karo and Hardy[11] was compared with the measurements.

To facilitate a comparison with impurity infrared absorption spectra, the perfect lattice density-of-states curve was obtained. In addition, the temperature dependence of the specific-heat Debye temperature and the reduced moments were calculated from temperature-dependent frequencies.

EXPERIMENTAL METHOD

One set of measurements, made with the Harwell Dido triple-axis spectrometer[9,12] employed the constant-$\mathbf{Q}$ mode technique[13] with an incident neutron energy of 56.67 meV. The measurements were made on a single crystal of NaBr 5 cm in diam. and 10 cm long,[14] mounted in an aluminum can to exclude water vapor. It was confirmed after the experiment that an insignificant amount of moisture had been absorbed. Because of the substantial incoherent scattering from the Na

† Work partially supported by U. K. A. E. A. Harwell Contract No. EMR/1778.

[1] B. Szigeti, Trans. Faraday Soc. **45**, 155 (1949). Proc. Roy. Soc. (London) **A204**, 51 (1950).

[2] R. P. Lowndes, Phys. Letters **21**, 26 (1966).

[3] Y. Pautamo, Ann. Acad. Sc. Fenn., AVI, **129**, 1 (1963).

[4] A. D. B. Woods, W. Cochran, and B. N. Brockhouse, Phys. Rev. **119**, 980 (1960); A. D. B. Woods, B. N. Brockhouse, R. A. Cowley, and W. Cochran, *ibid.* **131**, 1025 (1963).

[5] G. Dolling, R. A. Cowley, C. Schittenhelm, and I. M. Thorson, Phys. Rev. **147**, 577 (1966).

[6] G. Raunio, L. Almquist, and R. Stedman, Phys. Rev. **178**, 1496 (1969).

[7] H. G. Smith, R. M. Nicklow, P. R. Vijayaraghavan, G. Dolling, and M. K. Wilkinson, Bull. Am. Phys. Soc. **12**, 557 (1967).

[8] W. J. L. Buyers, Phys. Rev. **153**, 923 (1967).

[9] *Thermal Neutron Scattering*, edited by P. A. Egelstaff (Academic Press Inc., New York, 1965).

[10] J. S. Melvin, J. Pirie, and T. Smith, Phys. Rev. **175**, 1082 (1968).

[11] A. M. Karo and J. R. Hardy, Phys. Rev. **129**, 2024 (1963); University of California Report No. UCLR 14822, 1966 (unpublished); and private communication.

[12] D. H. Saunderson, C. Duffil, and R. I. Sharp, Atomic Energy Research Establishment Report No. R 4895, 1965 (unpublished).

[13] *Phonons*, edited by R. W. H. Stevenson (Oliver and Boyd, Edinburgh, 1966).

[14] Grown by Dr. D. A. Jones, Aberdeen University, using the Stockbarger method.

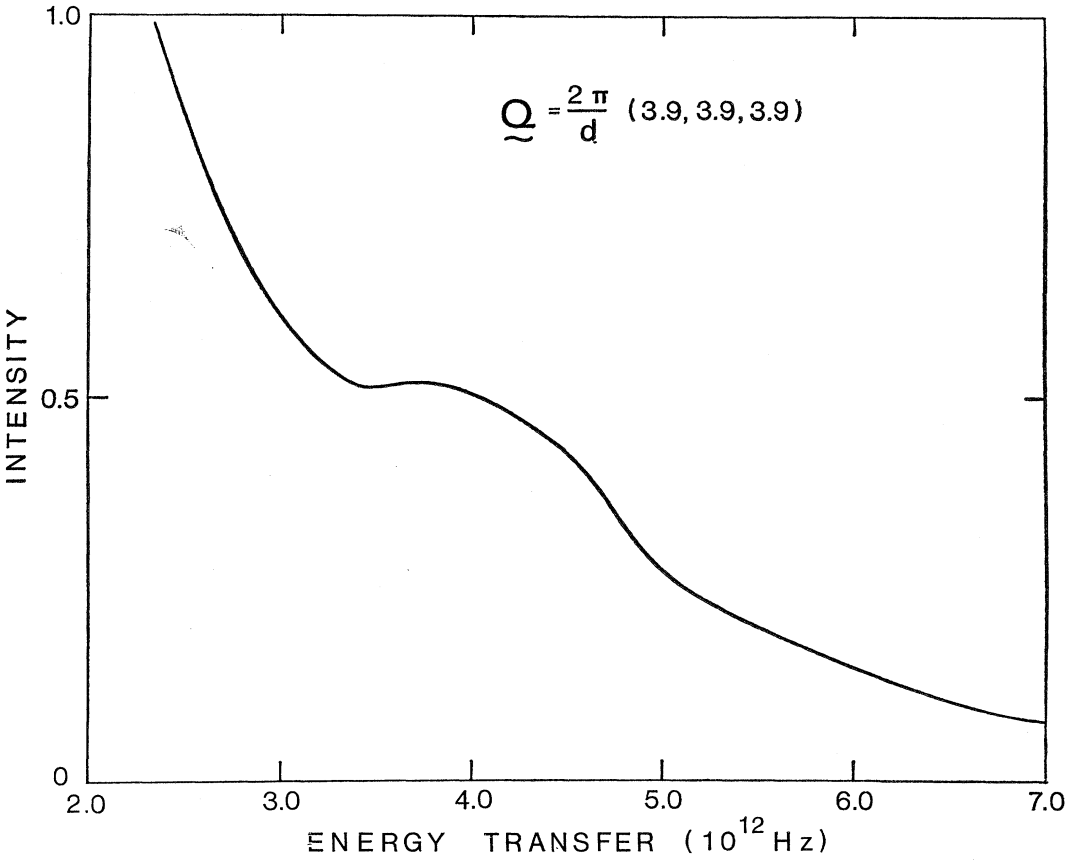

FIG. 1. Scattering intensity observed with the triple-axis spectrometer at $\mathbf{Q}=(3.9,3.9,3.9)\ 2\pi/d$ where no one-phonon peak occurs.

atom and the appreciable absorption cross section of the Br atoms, long counting times were necessary.

A second set of measurements was made on the Dido cold neutron time-of-flight spectrometer[15] at Harwell. The neutron flux from a liquid-hydrogen source was monochromated to a wavelength of approximately 4.1 Å and the scattered neutrons were timed over a flight path of 240 cm before being counted by one of the 24 scintillation counters. As a longer wavelength than that provided by the triple-axis spectrometer was used, the optimum crystal was now a cylinder of diameter 1.8 cm. A cylinder of this size was taken from the middle of the previous sample. From neutron Laue peaks, the mosaic spread was found to be between 0.5° and 1° and the [110] axis was 4.5° away from the cylinder axis. Runs were made with 13 different crystal orientations, each run lasting for 36 h.

All experimental measurements were made at 295°K.

ANALYSIS

For the triple-axis spectrometer measurements, the instrumental background noise (which was generally energy-dependent) was subtracted from the total scattering intensity. For some of the higher-frequency modes it was also necessary to subtract the intensity from scattering processes other than the single-phonon coherent process. The method adopted was to measure the scattering at a wave vector, $(3.9,3.9,3.9)\times 2\pi/d$, where no single-phonon coherent scattering was expected over the energy range of these modes. The incoherent and multiphonon scattering obtained in this way can be seen in Fig. 1. Although the wave-vector dependence of this sample scattering could have been calculated from a model, an adequate procedure for the present purpose of obtaining reliable one-phonon frequencies was to scale the sample scattering to the wings of each observed neutron group. The mean of the resultant one-phonon group obtained by subtraction of both instrumental and sample backgrounds was then taken as the phonon frequency. The statistical error associated with each frequency was the variance of the mean of the one-phonon (or signal) neutron group, given as[16]

$$\langle(\Delta\bar{E})^2\rangle=\frac{\sigma^2}{N}+\sum_i\frac{b_i(E_i-\langle E\rangle)^2}{N^2}+h^2\sum_i\frac{S_i^2}{12N^2},\quad(3)$$

[15] D. Harris, S. J. Cocking, P. A. Egelstaff, and F. J. Webb, in *Symposium on the Inelastic Scattering of Neutrons in Solids and Liquids, Chalk River, Canada, September, 1962* (International Atomic Energy Agency, Vienna, 1963), Vol. I, pp. 107–118.

[16] M. Kendal and A. Stuart, *The Advanced Theory of Statistics*, (Griffin and Co., London, 1958), Vol. 1.

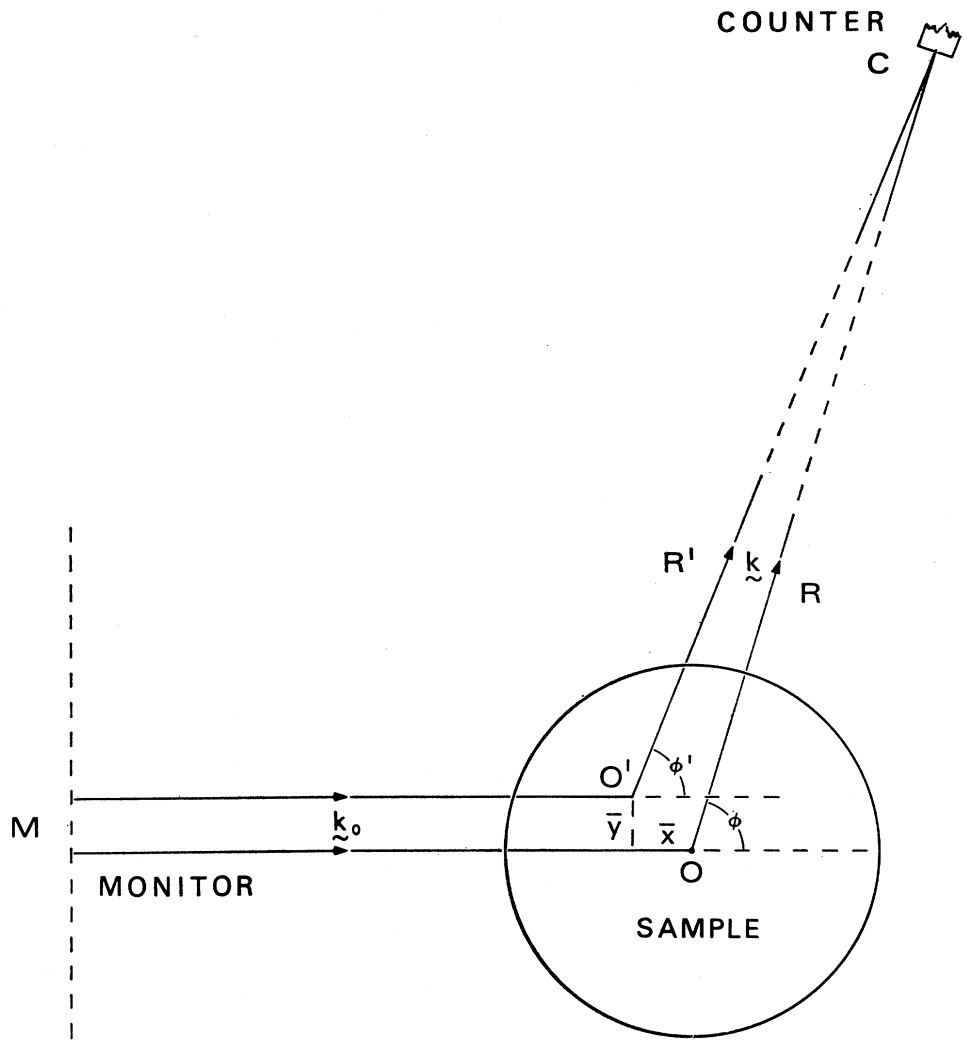

FIG. 2. Geometry of the time-of-flight experiment. O′ is the mean scattering center for the counter C and the scattered wave vector **k**.

where there were S_i signal counts and b_i background counts in the ith energy step. The value of h was approximately the energy resolution, the variance of the total neutron group was σ^2, and $N(=\sum_i S_i)$ was the number of signal counts in each group.

For the time-of-flight spectrometer there is a general reduction in the scattered intensity due to the larger absorption coefficient (14 b) at the longer neutron wavelength of 4.1 Å. This also causes the mean scattering point O' (Fig. 2) to be a function of the counter angle and the scattered energy. The position of O' was calculated by numerical integration for every counter position over the range of energies observed. Fortunately, the variation with energy for a given counter was small and for each counter an average position could be used. The value for OO' increased with scattering angle to 0.5 cm at 90°. From the positions of O' the corrected counter distances (R') and angles (ϕ') were obtained. Also, the mean time at which the incident beam arrived at the crystal depended on O' and hence was corrected for each counter.

A time-of-flight spectrum showing several typical features is given in Fig. 3. When evaluating the mean position of each single-phonon peak, all other prominent peaks in the spectrum were represented by Gaussians. Incoherent and multiphonon scattering were represented by up to four broader Gaussians and the instrumental background by a constant.

At the small values of $|\mathbf{K}|$ where most of the measurements were made, the background Gaussians represented mainly the incoherent scattering. The energy distribution varies slowly with position in reciprocal space and this (Fig. 4) was calculated from the best deformable dipole model[11] available at the time of the experiment. Although Fig. 4 indicates a large amount of scatter in the acoustic region it provides only a small background for a typical coherent acoustic-phonon peak. In the optic region, however, the incoherent

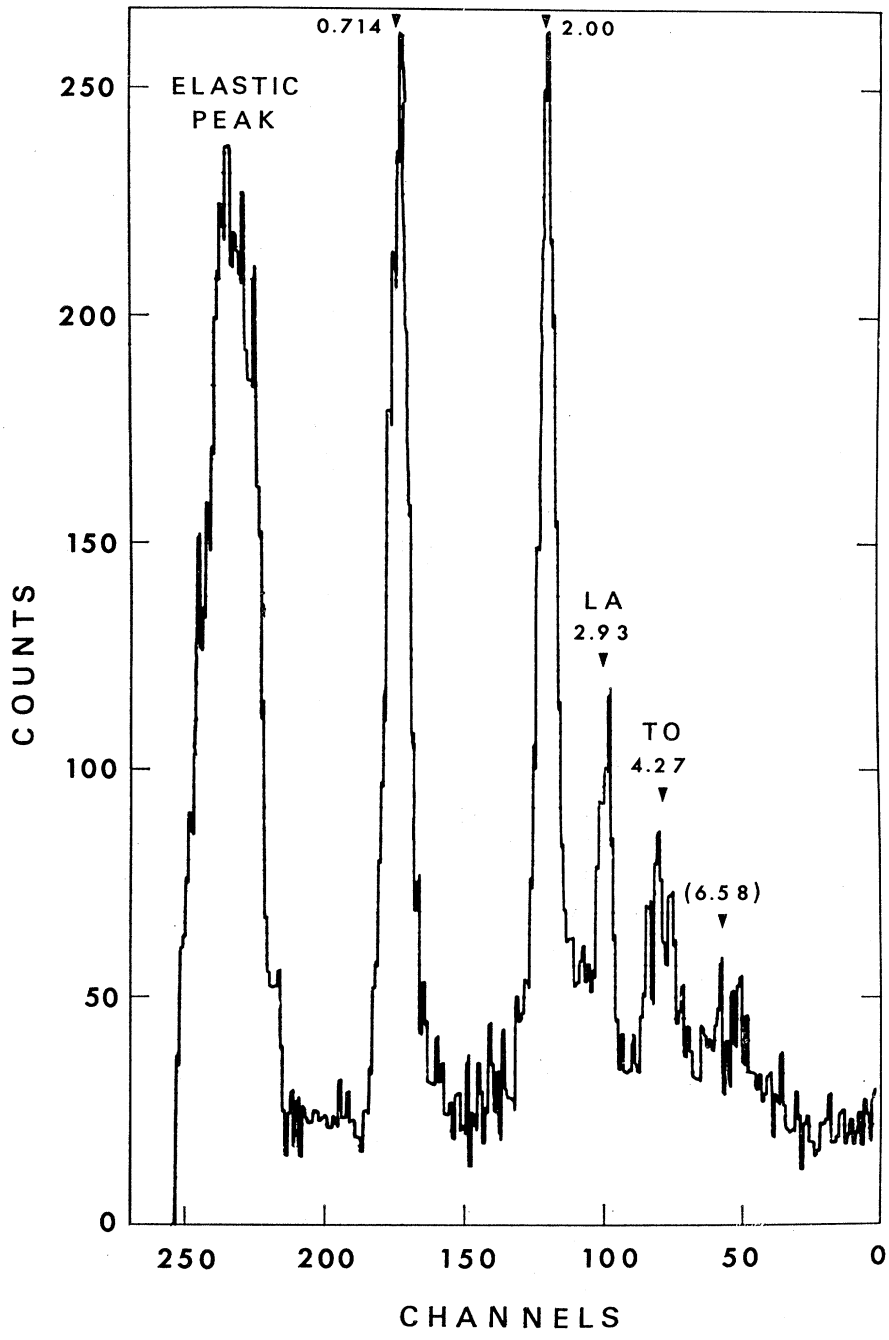

FIG. 3. Time-of-flight spectrum (the true origin is at −51.2 channels). The arrows indicate the mean peak positions, and the associated numbers give the frequency in 10^{12} Hz. The peak at 6.58 is caused by multiphonon scattering.

scatter is important. Using Fig. 4 as a guide, comparisons were made between neighboring spectra to obtain estimates of the background Gaussians. All these Gaussians were subtracted from the peak of interest whose mean was then evaluated. The variance of the mean was calculated from an expression similar to Eq. (3):

$$\langle(\Delta\bar{\tau})^2\rangle = \frac{\sigma^2}{N} + \sum_i b_i \frac{(\tau_i - \langle\tau\rangle)^2}{N^2} + \sum_i \frac{S_i^2}{12N^2}. \quad (4)$$

No second-order corrections were made to compensate for the nonlinearity of the instrumental resolution since Sinha[17] has demonstrated that these were generally small.

The final stage of the analysis consists in obtaining interpolated frequencies on symmetry directions. The phonon coordinates (Q_x,Q_y,ν) in reciprocal space can be divided into sets lying on scattering lines.[18] The inter-

[17] S. K. Sinha, Phys. Rev. **143**, 422 (1966).
[18] G. Placzek and L. Van Hove, Phys. Rev. **93**, 1207 (1954).

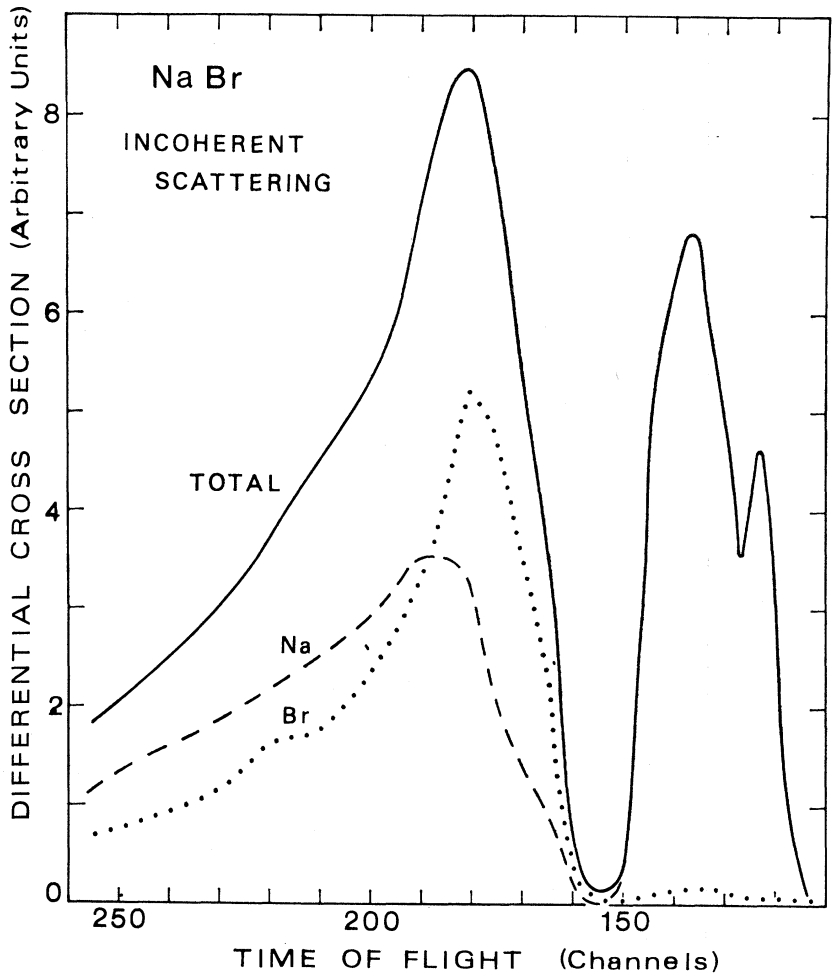

FIG. 4. Incoherent scattering cross section calculated from the DDNNN model and smoothed by instrumental resolution. The dotted curve gives the contributions of the Br atoms (which is negligible in the optic region) and the dashed curve, the contribution of the Na atoms.

section of these lines with the symmetry directions was calculated by interpolating Q_y against Q_x and ν against Q_x. This interpolation was performed by fitting increasing orders of a polynomial expansion to the points on a scattering line near the symmetry direction of interest until the resulting interpolation converged. It was found that no more than a fourth-degree polynomial was needed. The interpolated points were then reduced to equivalent points (q_i,ω) in the first Brillouin zone. The mean-square errors $\langle(\delta q_i)^2\rangle$ and $\langle(\delta\omega)^2\rangle$ were derived from the error $\langle(\Delta\tau)^2\rangle$ in the mean of the time-of-flight spectra. These errors were then reduced to a single error in q using the relation

$$\langle(\Delta\omega)^2\rangle=\langle(\delta\omega)^2\rangle+\sum_{i=1}^{3}\left(\frac{\partial\omega}{\partial q_i}\right)^2\langle(\delta q_i)^2\rangle. \qquad (5)$$

The graphs discussed in the next section show phonon frequencies as a bar with length the square root of $\langle(\Delta\omega)^2\rangle$ on either side of the mean frequency.

TABLE I. Phonon frequencies (10^{12} Hz) in NaBr along the radial symmetry directions. The measurements were made at 295°K.

Wave vector in units $(2\pi/d)$	Frequencies of normal modes LA	LO	TA	TO
(0.1,0.1,0.1)	1.005±0.025	6.20±0.10	0.706±0.015	4.05±0.05
(0.2,0.2,0.2)	1.805±0.03	6.12±0.10	1.255±0.02	4.04±0.05
(0.3,0.3,0.3)	2.54 ±0.035	5.98±0.10	1.70 ±0.02	3.98±0.07
(0.4,0.4,0.4)	3.02 ±0.035	5.82±0.10	2.01 ±0.03	3.85±0.06
(0.5,0.5,0.5)	3.15 ±0.03	5.73±0.10	2.13 ±0.03	3.81±0.05
(0.2,0.2,0)	1.49 ±0.04	5.89±0.15	0.86 ±0.015	4.05±0.07
(0.4,0.4,0)	2.54 ±0.04	5.54±0.15	1.65 ±0.03	4.10±0.08
(0.6,0.6,0)	2.76 ±0.11	5.00±0.15	2.20 ±0.03	4.20±0.09
(0.8,0.8,0)	2.31 ±0.07	4.48±0.10	2.63 ±0.03	4.25±0.10
(1.0,1.0,0)	1.72 ±0.03	4.20±0.10	2.74 ±0.03	4.17±0.10
(0.2,0,0)	1.26 ±0.015	6.09±0.14	0.591±0.01	4.03±0.06
(0.4,0,0)	2.26 ±0.03	5.40±0.15	1.06 ±0.025	4.04±0.06
(0.6,0,0)	2.85 ±0.03	4.55±0.08	1.44 ±0.03	4.06±0.08
(0.8,0,0)	2.92 ±0.03	4.24±0.08	1.70 ±0.03	4.16±0.08
(000)		6.22±0.12		4.04±0.06

RESULTS

The triple-axis spectrometer yielded 27 different phonons and the time-of-flight spectrometer gave some

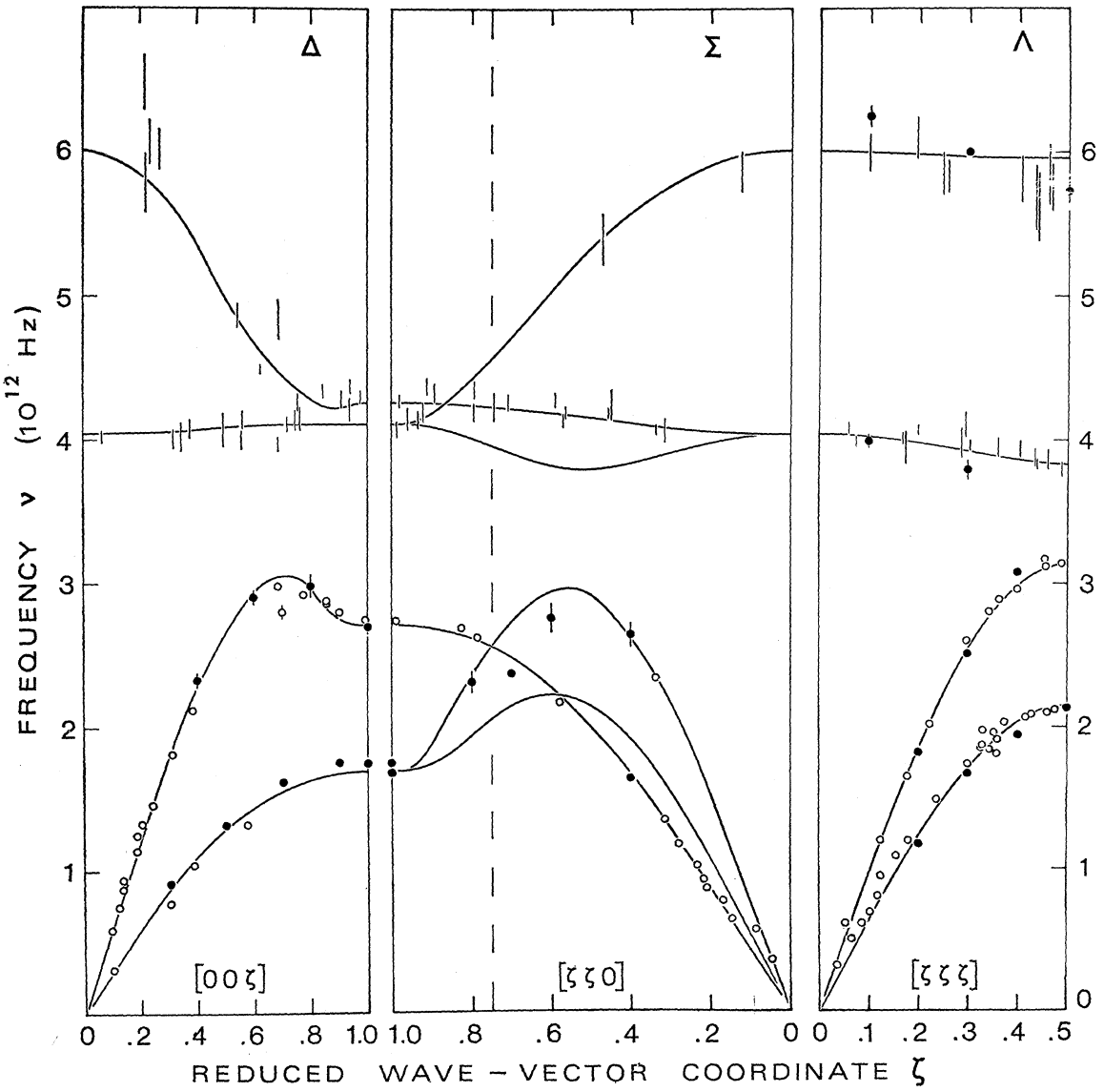

FIG. 5. NaBr dispersion curves given by model II. The time-of-flight frequencies are shown as bars and the triple-axis spectrometer measurements are distinguished by a central solid dot.

150 phonons along the symmetry directions. From this data, phonon frequencies were interpolated at intervals of $\frac{1}{5}q_{\max}$ to the zone boundary and are given in Table I.

TABLE II. Results of the least-squares-fitting procedures. Parameters varied during the fitting are those shown with error estimates. Model I is fitted to the triple-axis spectrometer measurements and models II–V to the complete set of data. Model II D is the deformable-shell model equivalent to model II with the additional fitted parameter $S=4.7\pm0.1$.

	Short-range forces ($e^2/2V$)					Polarizabilities				
NaBr 295°K Model	Nearest neighbors A	Nearest neighbors B	Second neighbors Bromine A″	Second neighbors Bromine B″	Ionic charge (e) Z	Electrical (10^{-24} cm³) α_+	Short range (e) d_+	Electrical (10^{-24} cm³) α_-	Short range (e) d_-	Goodness of fit X^2
I	11.05±0.06	−0.98±0.03	0	0	1	1.86±0.3	−0.17±0.01	3.89±0.15	0.14±0.01	1.19
II	11.39±0.06	−1.04±0.02	0	0	1	0.91±0.11	−0.16±0.01	3.94±0.05	0.19±0.01	1.80
III	11.49±0.10	−1.04±0.05	−0.22±0.07	0.05±0.04	1	0.96±0.16	−0.18±0.02	3.73±0.11	0.16±0.02	1.69
IV	10.33±0.65	−0.78±0.13	0.20±0.22	−0.02±0.04	0.92±0.04	0.38±0.27	−0.09±0.04	3.57±0.16	0.15±0.02	1.72
V	10.91±0.16	−0.88±0.05	0	0	0.96±0.01	0.64±0.11	−0.13±0.01	3.62±0.11	0.16±0.01	1.64
II D	11.42±0.06	−1.05±0.02	0	0	1	0.89±0.11	−0.16±0.01	3.92±0.05	0.19±0.01	1.81

Models Fitted to Measured Phonon Frequencies

These phonon frequencies of Table I were least squares fitted by a series of rigid-shell models,[19] in which translation of the shell relative to the core was the only ionic deformation allowed. The analysis and notation employed has been described by Buyers.[8] The model parameters derived are shown in Table II along with the goodness of fit X^2 defined as

$$X^2=\frac{1}{n(\text{expt})-N(\text{model})}\times\sum_{n(\text{expt})}\frac{[\nu^2(\text{model})-\nu^2(\text{expt})]^2}{\sigma^2(\nu^2(\text{expt}))},\quad(6)$$

where n(expt) is the number of experimental frequencies ν(expt), N(model) is the number of fitted model parameters, and σ^2 $(\nu^2(\text{expt}))$ the variance of ν^2(expt).

It may be seen that despite the large size of the Br^- ion, the introduction of the Br^--Br^- force constants A'' and B'' in model III only slightly changes the goodness of the fit. The poor agreement with the Szigeti relations[1] suggests a nonunit ionic charge, but again (model IV) only a small change is produced in the fit. Model II, which is shown in Fig. 5, is therefore considered the best model for NaBr as it has the merit of simplicity over the more complex and scarcely more accurate models III to V. For all the models the crystal polarizability of the Na^+ ion is negative, corresponding to a positive charge on the Na shell. This is in agreement with the unphysical sign of the polarizability of the positive ion found by similar analysis of KBr and NaI.[19] It is not possible to compare directly the parameters of the shell models for KBr and NaI, since there was no equivalent to our model II for these materials, and the measurements were not taken at room temperature. However, it can be seen[19] that the polarizabilities of the Na^+ and Br^- ions in NaBr are in reasonable agreement with the corresponding polarizabilities given by several models of KBr and NaI.

TABLE III. Macroscopic parameters derived from the fitted shell models.

Model	Optical frequencies (10^{12} Hz) ν_{TO} $(q=0)$	ν_{LO} $(q=0)$	Dielectric constant ϵ_∞	Elastic constants (10^{11} dyn/cm^2) C_{11}	C_{12}	C_{44}
I	4.03	6.14	3.29	4.31	0.87	1.14
II	4.04	6.01	2.66	4.55	0.92	1.10
III	4.05	6.06	2.61	4.50	0.76	1.07
IV	4.06	6.06	2.28	4.50	0.81	1.05
V	4.06	6.05	2.41	4.51	0.79	1.06
Experiment (see Table V)	4.05 4.04	6.26 6.22	2.62	4.006	1.045	0.996
Zero sound [Eq. (8)]				4.406	0.940	0.996

TABLE IV. Values of X^2 and input parameter specifications for the shell models fitted to macroscopic constants.

Model	Type	Polarizable ions		Determining parameters	X^2
DDNNN	deformable dipole	Na	Br	a	17.6
1	rigid shell		Br	b	16.8
2	rigid shell	Na	Br	c	21.4
3	deformable shell		Br	d	8.7
4	rigid shell		Br	e	13.9
5	deformable shell		Br	f	9.3
6	rigid shell		Br	g	13.0
7	deformable shell		Br	h	14.1

[a] Reference 11.
[b] C_{11}, C_{12}, C_{44}, ϵ_0, ϵ_∞, ν_{TO}—Table V.
[c] As Ref. b plus α_+, α_-—Table V.
[d] As Ref. b with $S=0.27$—Eq. (7).
[e] As Ref. b but with $\Delta C_{11}=0.1\ C_{11}$, $\Delta C_{12}=-0.1\ C_{12}$.
[f] As Ref. e with $S=0.27$.
[g] As Ref. b but with 4°K values of C_{11}, C_{12}, C_{44}—Table V.
[h] As Ref. g with $S=0.27$.

In order to find how well the dispersion curves are defined by the restricted set of mainly acoustic phonons derived from the triple-axis spectrometer measurements, the models were fitted to this data only. It was again found that the best model involved six parameters like model II and the results are given as model I in Table II. Although some of the parameters of model I differ significantly from those of model II, only minor changes occur in the resulting dispersion relations as may be seen from the solid curves in Fig. 6. The smaller value of X^2 obtained for model I arises largely because the mainly acoustic data used in this model are easier to fit. When the full data is used the largest contributions to X^2 come from the LO modes, particularly in the [111] direction as may be seen from Fig. 5. Similar difficulties in fitting the optic modes are also found for the more complex models III to V.

The comparison in Table III of the macroscopic predictions of the fitted models with the measured optical crystal properties shows that excellent agreement exists for the optical modes, and fair agreement for the dielectric constant. For the elastic constants, however, systematic differences exist between all model predictions and the values obtained at long wavelengths by ultrasonic techniques. For example, the value of C_{11} is greater than the ultrasonic value, being 13% higher for model V. This is a similar discrepancy to that found by Buyers[8] in NaF and represents a 6% difference in the slope of the LA branches in the [100] direction. Also the wrong sign is obtained for the Cauchy difference $(C_{12}-C_{44})$. In fact, the elastic constants are nearer to the zero-sound[20] values estimated in the next section than they are to the ultrasonic (first sound) values. That such a difference between first-sound and zero-sound elastic constants exists was first demonstrated

[19] R. A. Cowley, W. Cochran, B. N. Brockhouse, and A. D. B. Woods, Phys. Rev. **131**, 1030 (1963).

[20] R. A. Cowley, Proc. Phys. Soc. (London) **90**, 1127 (1967).

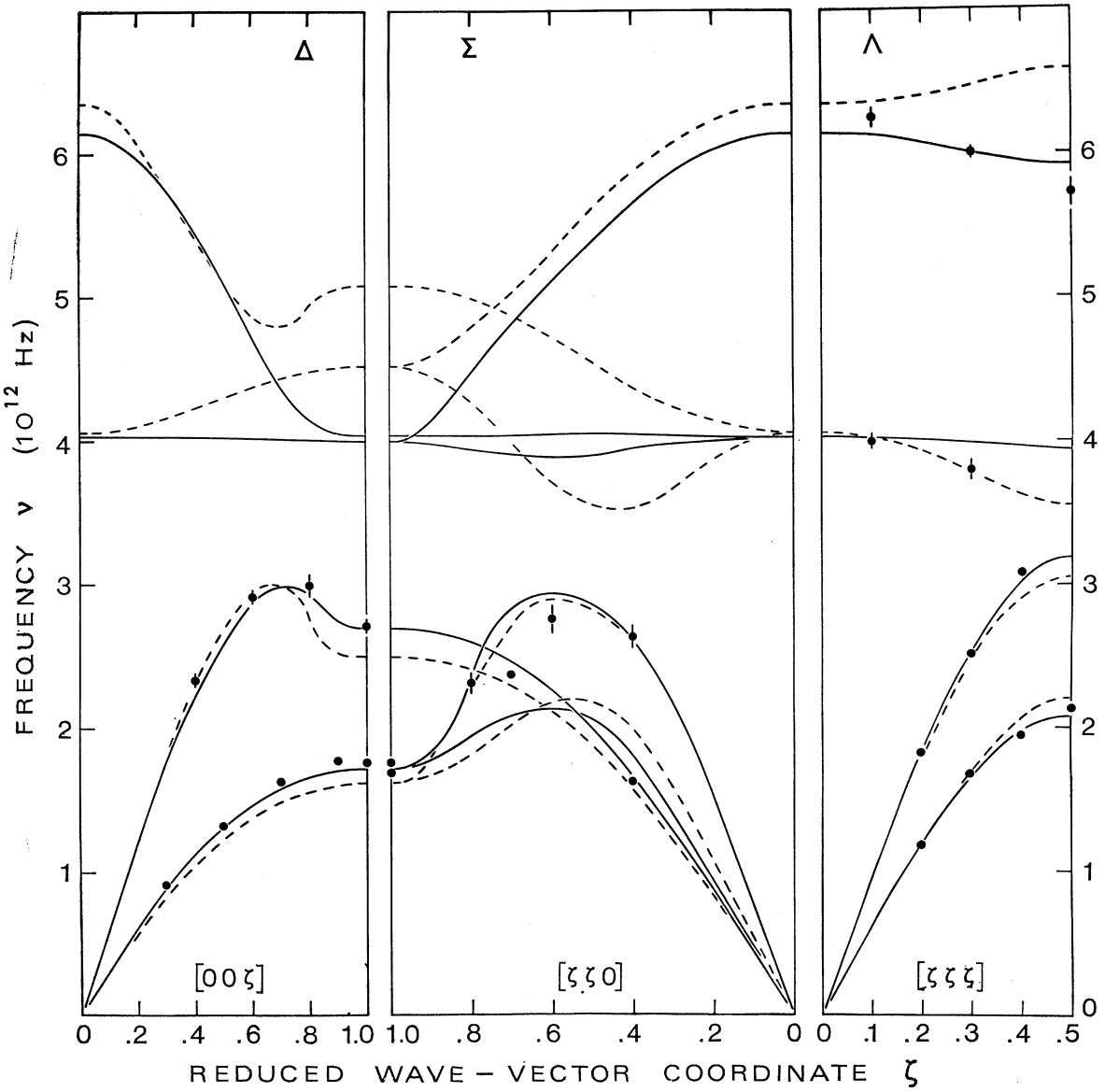

FIG. 6. Frequencies of phonons at 295°K in NaBr obtained by the triple-axis spectrometer. The dashed lines are given by the DDNNN model and the solid lines by the model I, which was fitted to the phonon frequencies shown. The length of each line represents twice the standard deviation in the frequencies.

for KBr[21] and is likely to be the source of the discrepancies found in both NaF and NaBr.

Least-squares fitting procedures have been developed for deformable-shell models[10] where the outer electron shell was allowed to deform radially. For the simple deformable-shell model, and for the deformable-shell model,[10] one extra parameter

$$S=\tfrac{1}{3}k^r(2)/k(2) \qquad (7)$$

is sufficient to describe the radial rigidity, where $k^r(2)$ is the radial shell-core spring constant of the negative ion, and $k(2)$ its translational spring constant.[10] The result for model II D, which is the deformable-shell equivalent of model II, is typical of several models and can be seen in Table II. The best fitted value of S (4.7) corresponds to a negligible radial deformation (a significant value would be less than or equal to unity). Since the incorporation of the radial degree of freedom has led to no decrease in X^2, there is no advantage in including radial deformation when fitting shell models to dispersion curves in crystals analogous to NaBr.

Models Fitted to Macroscopic Data

In this section the dispersion curves predicted from macroscopic constants by a number of models are compared with the experimental measurements.

[21] E. C. Svensson and W. J. L. Buyers, Phys. Rev. 165, 1063 (1968).

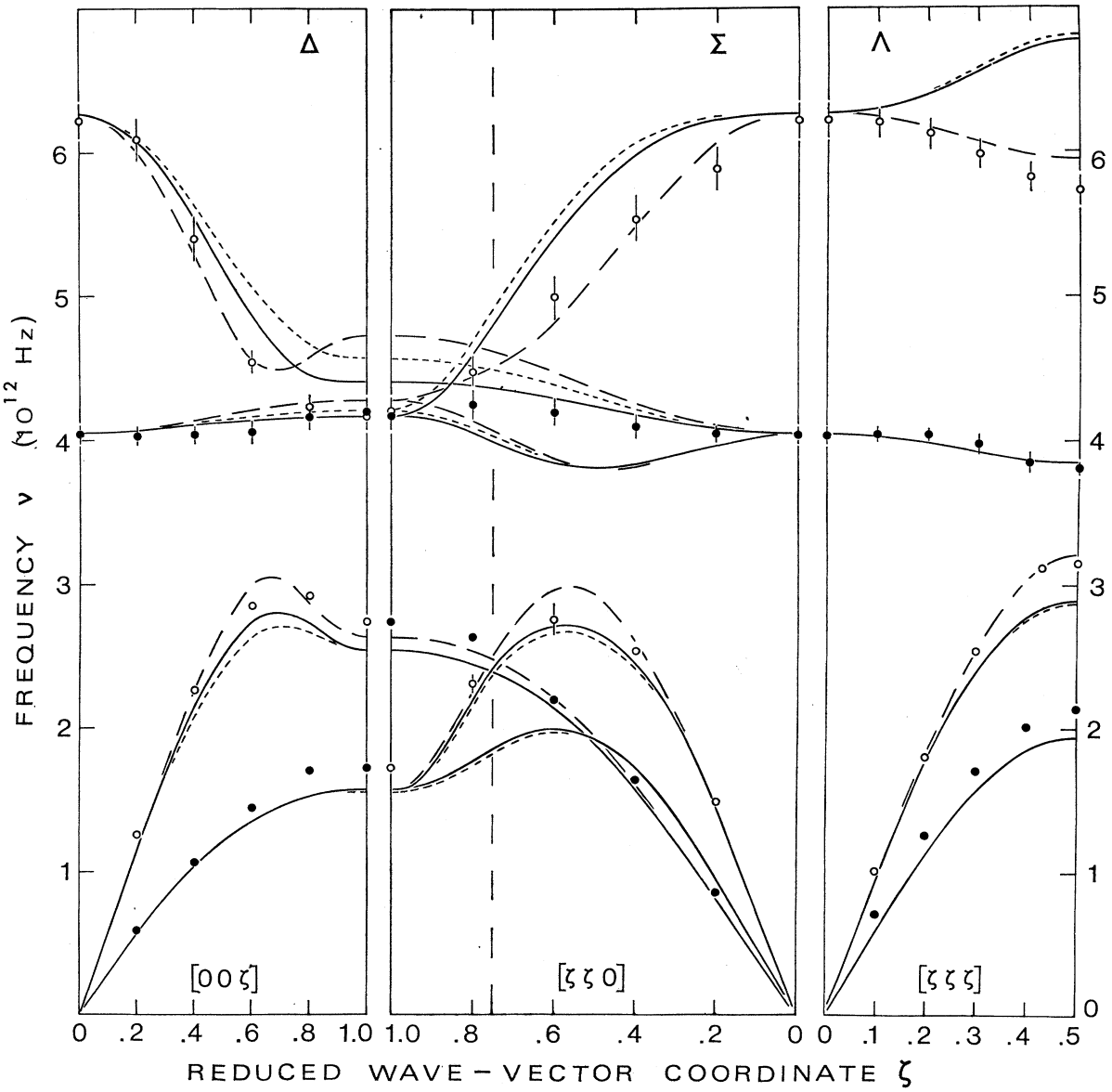

FIG. 7. NaBr dispersion curves given by models fitted to macroscopic parameters. Solid lines are frequencies from model 1 (see Table IV); dashed lines are frequencies from model 2 (see Table IV); dotted lines are frequencies from model 3 (see Table IV). The open and solid circles are the longitudinal and transverse frequencies derived from the measurements at intervals of $\frac{1}{5}\zeta_{\max}$ (Table I).

The deformation dipole (DD) models of Karo and Hardy[11] have been used to predict the phonon frequencies from macroscopic data. The frequencies (private communication) of the model with second-neighbor forces DDNNN are an improvement over those derived from the DD model[11] which has only first-neighbor forces. They are shown in Fig. 6. The observed TO branches are much flatter than the predictions and in all branches the discrepancies increase near the zone boundaries. Smaller effects of the same general character have been noted in NaF by Buyers[8] and are found also when deformable-dipole model predictions are compared with the experimental measurements of KBr and NaI.[4] The value of X^2 for the DDNNN model for NaBr is given in Table IV.

Predictions have also been made from macroscopic data using rigid-shell models with second-neighbor forces between anions, a noncentral first-nearest-neighbor force, and unit ionic charges. The dispersion curves with both ions polarizable (model 2) and with the bromine ion only polarizable (model 1) are shown in Fig. 7. Values of X^2 and details of the input parameters are in Table IV. As in other alkali halides[10] the best predictions (lowest X^2) are obtained when one ion is polarizable. Hence, in the following, the results from models with only the negative ion polarizable will be

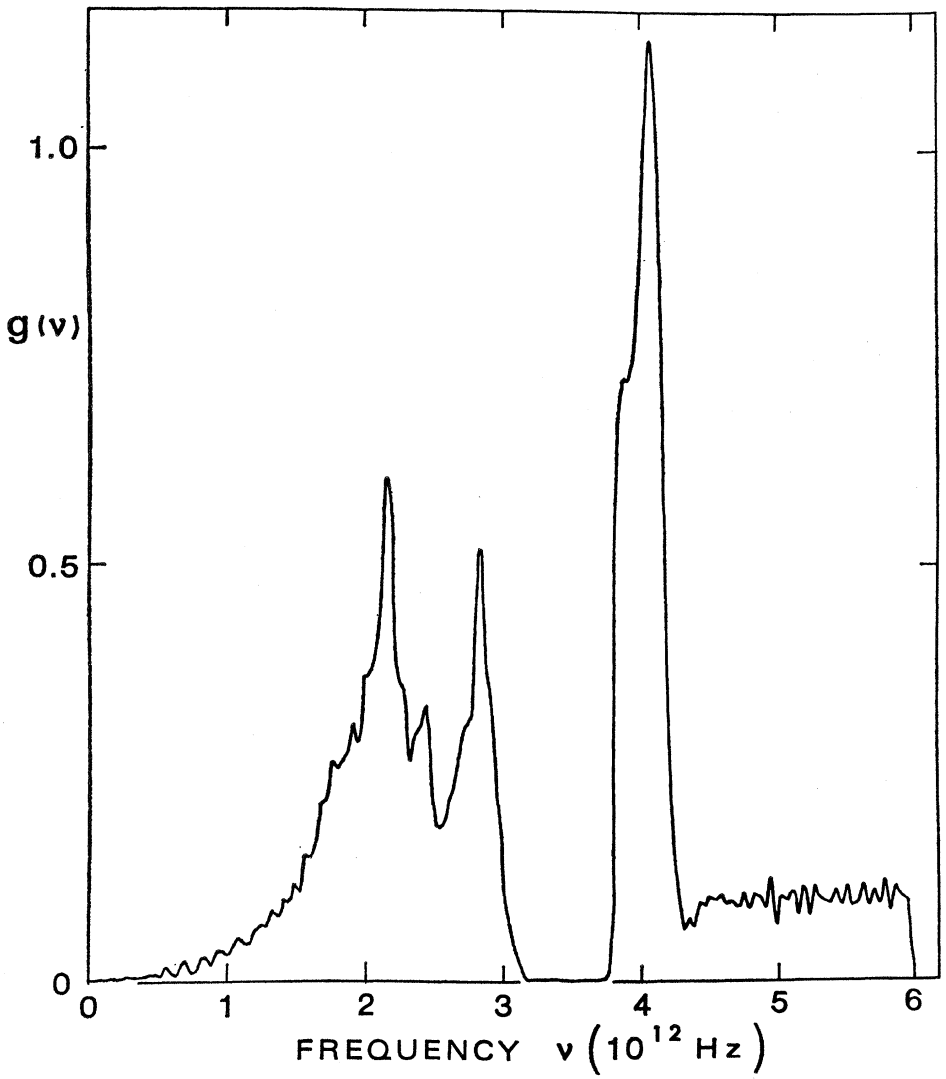

FIG. 8. Normalized frequency distribution of NaBr given by model II.

discussed. From Fig. 7 one can see that the discrepancies are greatest near the zone boundaries. This is again most noticeable in the [111] direction where only one type of atom is in motion and the model reduces to the (unsatisfactory) model with rigid ions. In fact, it was found impossible to reproduce the decrease in frequency of the [111] LO branch with increasing wave vector by any rigid-shell model fitted to the macroscopic constants.

For the simplest form of a deformable-shell model (the simple deformable-shell model[10]) no parameters are required in addition to those of the corresponding rigid-shell model, and $S=1$. The dispersion curves show some improvement but better results are obtained from the deformable-shell model in which a greater degree of radial distortion ($S=0.27$ as used for the sodium halides in Ref. 10) is allowed (model 3). The curves are given in Fig. 7 and although the over-all improvement is substantial, with X^2 reduced to 8, an anomaly is introduced in the LO optic branch near the [100] zone boundary. This is a feature of deformable-shell models and is not due to uncertainty in the defining macroscopic data.

All the dispersion curves so far discussed in this section were obtained from the ordinary (first sound) elastic constants, but at room temperature the elastic constants are almost certainly close to the zero-sound elastic constants. The difference between the first- and zero-sound elastic constants has been calculated[20] in the long-wavelength limit only for KBr and NaI. Since similar information is not available for NaBr, rough estimates were made of the zero-sound elastic constants assuming the effect was similar in magnitude to that in KBr and NaI. Changes of

$$\Delta C_{11}/C_{11}=0.1,\quad \Delta C_{12}/C_{12}=-0.1,\quad \Delta C_{44}/C_{44}=0.0 \quad (8)$$

were assumed. Models 4 and 5 (Table IV) are equivalent to models 1 and 3 but with these modified elastic constants. As an alternative, in models 6 and 7

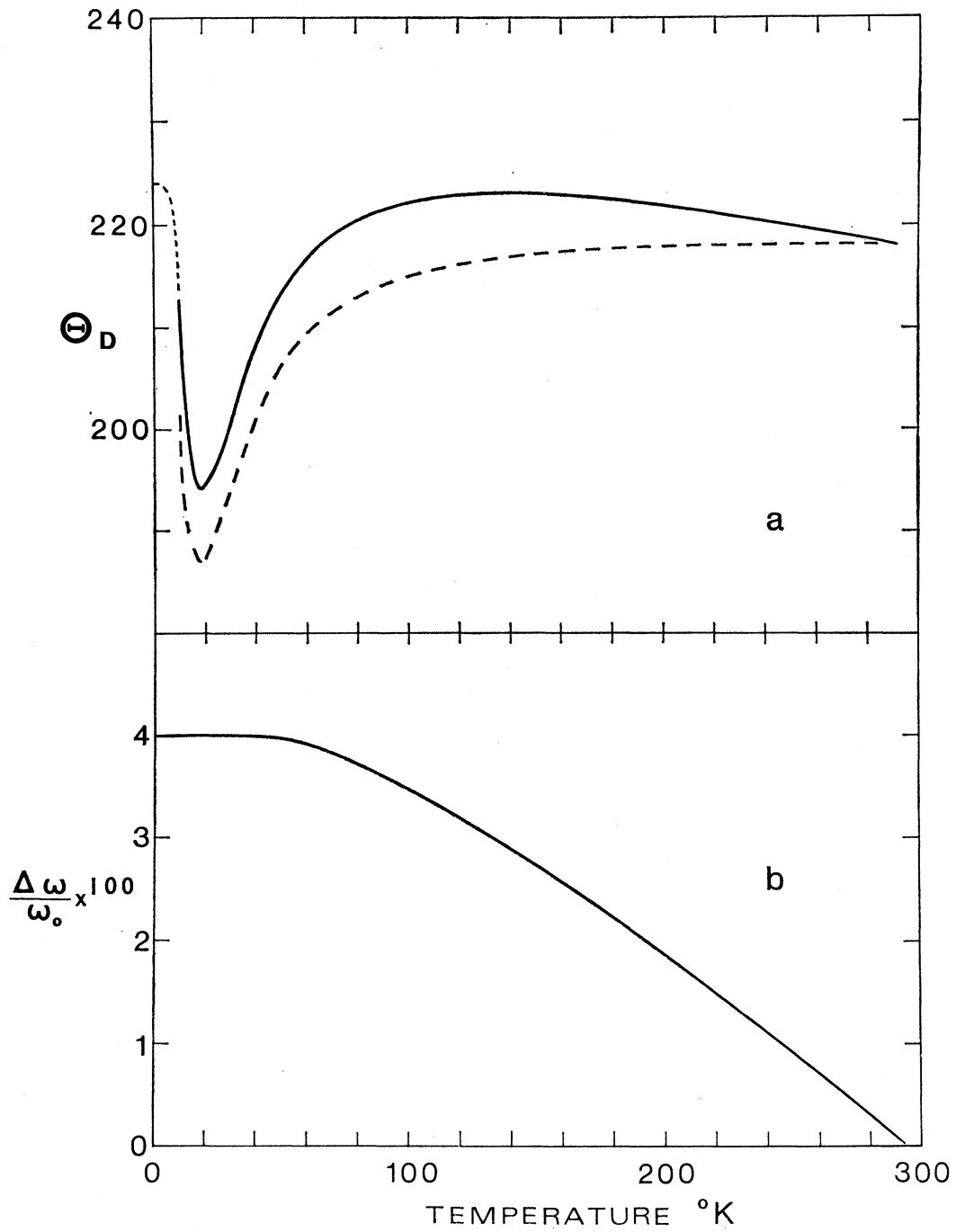

FIG. 9. (a) Specific-heat Debye temperature Θ_D of NaBr as a function of temperature. The dashed curve is calculated from the frequency distribution of model II at 295°K and the solid curve makes an allowance for temperature-dependent frequencies. The value at 0°K is derived from the elastic constants. (b) Mean shift in frequencies used to correct the frequency distribution as a function of temperature.

the elastic constants measured at 4°K (Table V) were used as an estimate for the room-temperature zero-sound elastic constants. None of these models provides a much better over-all fit than those previously considered, but for all the models there is some improvement in the acoustic branches. For the deformable-shell models, however, the anomaly at the [100] zone boundary increases. It is concluded that uncertainty in the estimation of the anharmonic contributions to the elastic constants does not substantially change the main

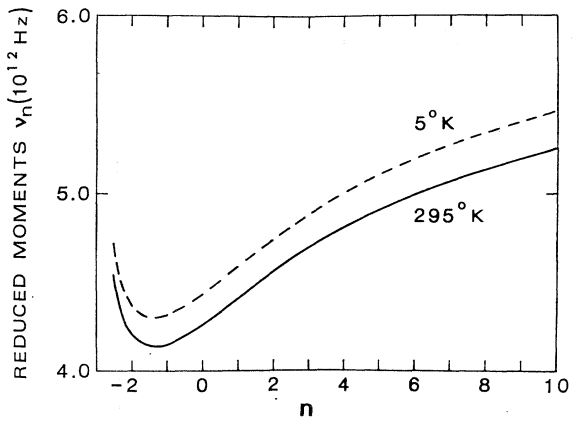

FIG. 10. Reduced moments of (a) the frequency distribution at 295°K (solid line) and (b) the modified distribution at 5°K (dashed line).

features of agreement between the measured frequencies and the dispersion curves predicted from rigid- and deformable-shell models.

DERIVED PROPERTIES

The vibrational spectrum obtained from the best fitted model (II) has been used to obtain the density-of-states distribution. Although recent techniques[22] give the distribution with almost arbitrary accuracy, in the present calculation the simpler frequency sampling method was used. A sample of 64 000 equally spaced wave vectors, containing 384 000 frequencies, in the Brillouin zone was sorted into 500 frequency intervals. Figure 8 shows the resulting distribution. The character of the distribution is similar to that of NaI and KBr but is very different from that given by the DDNNN model for NaBr. The sharp peak near 4.0×10^{12} Hz arises from the flat TO modes. A band gap between the acoustic and optic region is found between 106 and 125 cm^{-1}. The estimated gap of 90 to 130 cm^{-1} obtained by Metselaar and van der Elsken[23] is in reasonable agreement with this value.

TABLE V. Experimental data for NaBr.

		Experimental values 295°K	4°K
d	(Å)	5.97324[a]	5.926[b]
C_{11}	(10^{11} dyn/cm^2)	4.006[c,d]	4.800[c]
C_{12}	(10^{11} dyn/cm^2)	1.045[c,d]	0.986[c]
C_{44}	(10^{11} dyn/cm^2)	0.996[c,d]	1.070[c]
ϵ_0		6.28[e]	5.78[e]
ϵ_∞		2.62[f]	
α_+	(10^{-24} cm^3)	0.255[g]	
α_-	(10^{-24} cm^3)	4.130[g]	
$\nu_{TO_{q=0}}$	(10^{12} Hz)	4.05[f]	
		4.04[h]	
$\nu_{LO_{q=0}}$	(10^{12} Hz)	6.26[i]	
		6.22[h]	
ρ	(g/cm^3)	3.204[c]	3.299[c]

[a] R. W. G. Wyckoff, *Crystal Structures* (Wiley-Interscience, Inc., New York, 1951), Vol. I.
[b] Reference 3.
[c] J. T. Lewis, A. Lehoczky, and C. V. Briscoe, Phys. Rev. **161**, 877 (1967).
[d] S. Haussühl, Z. Physik, **159**, 223 (1960).
[e] Reference 2.
[f] D. H. Martin, Advan. Phys. **14**, 39 (1965).
[g] J. Tessman, A. H. Kahn, and W. Shockley, Phys. Rev. **92**, 890 (1953).
[h] This work.
[i] Calculated using the Lyddane-Sachs-Teller relation, R. H, Lyddane, R. G. Sachs, and G. Teller, Phys. Rev. **59**, 673 (1941).

[22] G. Gilat and L. J. Raubenheimer, Phys. Rev. **144**, 390 (1966).

The specific-heat Debye temperature $\Theta_D(T)$ was calculated from the frequency distribution [dashed curve of Fig. 9(a)]. An improved estimate using temperature-dependent quasiharmonic frequencies is shown by the solid curve of Fig. 9(a). The mean change in the quasiharmonic frequencies is shown in Fig. 9(b) and was obtained by a method to be described elsewhere.[24] The value of $\Theta_D(T)$ at 0°K was calculated from the low-temperature elastic constants. Although the specific heat has not been measured for NaBr the increase from room temperature to $\frac{1}{2}\Theta$ is expected from the behavior of other alkali halides.

The reduced moments defined as

$$\nu_n=[(n+3)\mu_n/3]^{1/n}, \tag{9}$$

when

$$\mu_n=\int \nu^n g(\nu)\,d\nu \Big/ \int g(\nu)\,d\nu \tag{10}$$

have been calculated using both the frequency distribution at 295°K and the estimated distribution at 5°K. The resulting curves are shown in Fig. 10.

ACKNOWLEDGMENTS

The authors wish to thank the Harwell P. N. R. Group for their invaluable assistance during the measurements. It is also a pleasure to thank Dr. A. Millington and Dr. R. I. Sharp for their advice and help with the time-of-flight spectrometer, and G. Peterson for reducing much of the triple-axis spectrometer data. We are indebted to Dr. J. M. Karo and Dr. J. R. Hardy for supplying unpublished eigendata, and to Dr. A. D. Jones for growing the single crystal. One of us (J.S.R.) is grateful to the Carnegie Trust for the award of a scholarship.

[23] R. Metselaar and J. van der Elsken, Phys. Rev. **165**, 359 (1967).
[24] J. S. Reid and T. Smith (unpublished).